ADVANCED FUNCTIONAL MATERIALS
www.afm-journal.de

Epitaxial Magnetic Oxide Nanocrystals Via Phase Decomposition of Bismuth Perovskite Precursors

*Kashinath A. Bogle, Jeffrey Cheung, Yong-Lun Chen, Sheng-Chieh Liao, Chih-Hung Lai, Ying-Hao Chu, John M. Gregg, Satishchandra B. Ogale, and Nagarajan Valanoor**

The phase instability of bismuth perovskite ($BiMO_3$), where M is a ferromagnetic cation, is exploited to create self-assembled magnetic oxide nanocrystal arrays on oxide supports. Conditions during pulsed laser deposition are tuned so as to induce complete breakdown of the perovskite precursor into bismuth oxide (Bi_2O_3) and metal oxide ($M\text{-}O_x$) pockets. Subsequent cooling in vacuum volatizes the Bi_2O_3 leaving behind an array of monodisperse nanocrystals. In situ reflective high energy electron diffraction beam is exploited to monitor the synthesis in real-time. Analysis of the patterns confirms the phase separation and volatization process. Successful synthesis of $M\text{-}O_x$, where M = Mn, Fe, Co, and Cr, is shown using this template-free facile approach. Detailed magnetic characterization of nanocrystals is carried out to reveal the functionalities such as magnetic anisotropy as well as larger than bulk moments, as expected in these oxide nanostructures.

1. Introduction

Self-organized magnetic metal oxide ($M\text{-}O_x$) nanostructures show tremendous potential in technological applications such as non-volatile random access memories,[1–3] magnetic recording media,[4] biosensors,[5] photocatalysis as well as energy conversion.[6–9] The properties of these nanostructures depend significantly on nanostructure morphology as well as orientation.[10–15] Whilst soft-chemistry derived methods to generate freestanding nanostructures are now relatively mature,[16–19] facile methods that offer epitaxial control with respect to an underlying substrate are still nascent. Typically oxide supported epitaxial nanostructure arrays offer two significant advantages compared to free-standings nanostructures. Firstly, by controlling the interface properties such as crystallographic orientation, lattice mismatch, defect density etc, one is able to distinctly decouple interfacial and bulk properties without compromising one another. Secondly, functional behavior associated with electronic[20] or magnetic[21] or catalytic[22] properties and linked to specific surface orientations and directionalities can be selectively amplified using accurately controlled synthesis.

Concurrently, bismuth-based perovskite ($BiMO_3$) thin films, where M is a cation with magnetic properties, have recently gained significant attention due to their prominent magnetoelectric or multiferroic effect.[23,24] One major finding in the intense search for successful synthesis of such multiferroics is that the growth-window (in terms of temperature, pressure and precursor-chemistry) to generate phase pure perovskites is very tight.[25–27] Even the slightest variation in the deposition conditions can change the resultant phase from single phase epitaxial $BiMO_3$ to a complex matrix of $Bi_z\text{-}M_y\text{-}O_x$ phase that coexists with pockets of epitaxial $M\text{-}O_x$.[27] This poses a tantalizing question: is it possible to exploit this phase sensitivity coupled with the intrinsically volatile nature of Bi_2O_3 to create monodisperse epitaxial $M\text{-}O_x$ nanocrystal arrays?

In this report we demonstrate how this inherent phase sensitivity of $BiMO_3$ and it's related chemistry during synthesis can be exploited to create a universal facile route for the generation of epitaxial magnetic oxide nanocrystals on a variety of orientations. We show successful synthesis of $M\text{-}O_x$ where M = Mn, Fe, Co and Cr. Although we have reported a detailed study of using this approach to fabricate Mn_3O_4 nanocrystal arrays,[28] this is the first time this technique is shown viable as a generic method to synthesize a wide range of magnetic metal oxides. Indeed this method has also been extended for the synthesis of other magnetic and transition metal oxide nanostructures. Detailed magnetic characterization of nanocrystals is carried out to reveal magnetic functionalities such as anisotropy as

Dr. K. A. Bogle, J. Cheung, Prof. N. Valanoor
School of Materials Science and Engineering
University of New South Wales
Sydney 2052, Australia
E-mail: nagarajan@unsw.edu.au
Y.-L. Chen, Y.-H. Chu
Department of Materials Science and Engineering
National Chiao Tung University
Hsinchu, 30010, Taiwan
S.-C. Liao, C.-H. Lai
Department of Materials Science and Engineering
National Tsing Hua University
Hsinchu, 30013, Taiwan
Prof. J. M. Gregg
Centre for Nanostructured Media
School of Maths and Physics
Queen's University Belfast
Belfast, BT7 1NN, N. Ireland, UK
Prof. S. B. Ogale
Physical and Materials Chemistry Division
National Chemical Laboratory
Pune, 411008, India

DOI: 10.1002/adfm.201201066

well as moments, which are significantly different from bulk in these oxide nanostructures.

2. Results and Discussion

It is first critical to understand the role of the bismuth-based precursor in our proposed technique. $BiMO_3$ perovskite synthesis demands a very narrow window as well as tight control of the deposition conditions during thin film growth process. Fujino et al.[25] reported that varying deposition oxygen partial pressure during synthesis of $BiMnO_3$ thin films displays the coexistence of $BiMnO_3$ phase along with patches of epitaxial Mn_3O_4. In the case of $BiFeO_3$, the most popular of multiferroics, non-optimal parameters of substrate temperature and chamber oxygen partial pressure leads to the formation of parasitic Fe_2O_3 phases in the film.[26,29] Langenberg et al. found parasitic phases of Mn_3O_4, Bi_2O_3 and $Bi_3Mn_4O_{10}$ along with $BiMnO_3$ when the substrate temperature was varied between ± 50 °C.[22] Based on a number of such reports and results from over 100 synthesis trials within the laboratory, we then created a temperature-pressure phase diagram (**Figure 1**) (a first such developed) where the symbols in the phase diagram indicate actual data points. This phase diagram reveals three key regions: i) $M\text{-}O_x$ phases (found to be stable at low oxygen pressure throughout the temperature range), ii) phase pure $Bi\text{-}M\text{-}O_x$ are formed close to chamber oxygen pressure of 10–2 mbar and substrate temperature in the range from 500 to 750 °C and iii) bismuth rich $M\text{-}O_x$ phases ($Bi_2O_3/M\text{-}O_x + Bi_z\text{-}M_y\text{-}O_x$).

Generally, at lower temperature or higher pressure, Bi_2O_3 precipitates while at lower pressure and higher temperature, $M\text{-}O_x$ forms. This diagram shows that conditions such as low oxygen pressure or high temperature, represented by brown region, generate either parasitic $M\text{-}O_x$ phases in the film or result in porous $M\text{-}O_x$ films. This is due to the high vapor pressure of both Bi and Bi_2O_3.[25,26,29] On the other hand higher oxygen pressures (blue region) coupled with relatively lower temperatures either induce the formation of Bi_2O_3 along with $M\text{-}O_x$ or compounds with Bi to M ratio (z/y) higher than 1. This is because of the oxidization of the excess bismuth ablated from the target into a stable Bi_2O_3 phase.[30] Finally there is a narrow window of processing conditions, represented by green region, to obtain phase pure $Bi\text{-}M\text{-}O_x$.

Whilst clearly illustrating the difficulty in obtaining single phase $Bi\text{-}M\text{-}O_x$ thin film, Figure 1 also reveals a new opportunity. The range for complete phase separation of $Bi\text{-}M\text{-}O_x$ into Bi_2O_3 and $M\text{-}O_x$ runs over a favorably wide range of growth conditions. We show how the perovksite phase instability coupled with the intrinsically volatile nature of Bi_2O_3 offers the grower an innovative new strategy to fabricate arrays of monodisperse individual nanocrystals. Since this method hinges on the phase instability of the parent bismuth-based precursor it is completely different from elastic motifs previously explored for the growth of metal oxide nanostructures.[16,18,31]

As illustrated in **Figure 2**, the first two steps (a and b) of our process entail the deposition of the $Bi\text{-}M\text{-}O_x$ precursor under appropriate conditions that induce phase separation. Figure 1 suggests that such condition is typically found in oxygen rich environment at high substrate temperature, where oxygen

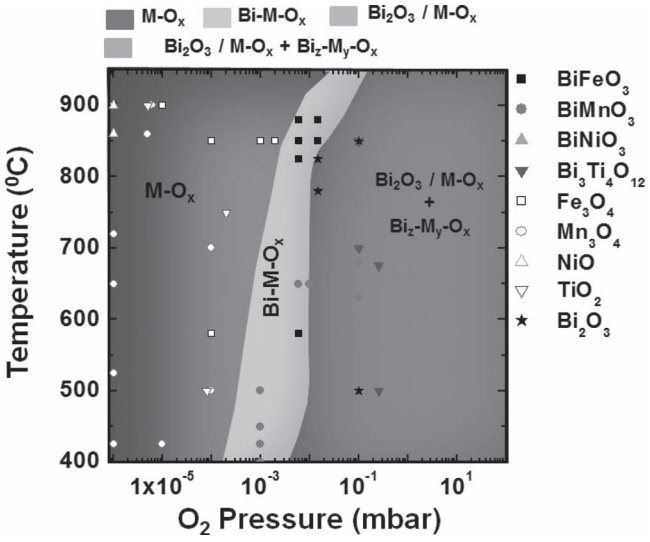

Figure 1. Schematic representation of temperature-pressure phase diagram for $Bi\text{-}M\text{-}O_x$ systems.

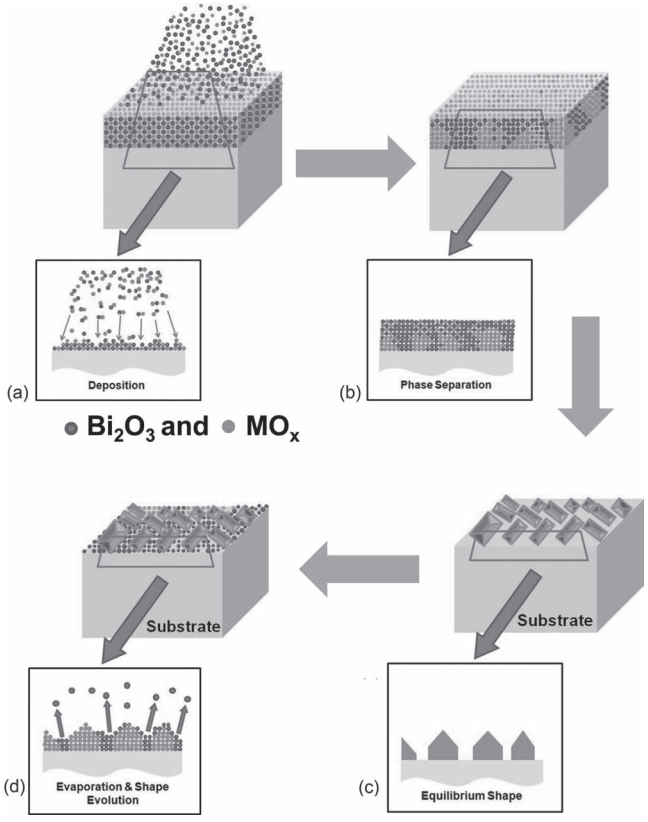

Figure 2. Schematic representation of universal process for fabrication of epitaxial M-Ox nanostructure on STO substrate. a) A layer of $BiMO_3$ is deposited from target on (001)-$SrTiO_3$ substrate via PLD under appropriate conditions. b) Induced phase seperation in the film. During phase separation the Bi_2O_3 and $M\text{-}O_x$ phases are expected to nucleate throughout the film and form dispersed pockets of nanometric size clusters. c) Subsequent cooling of the film in high vacuum vapourizes Bi_2O_3. d) After cooling the $M\text{-}O_x$ phase acquires thermodynamically stable shape.

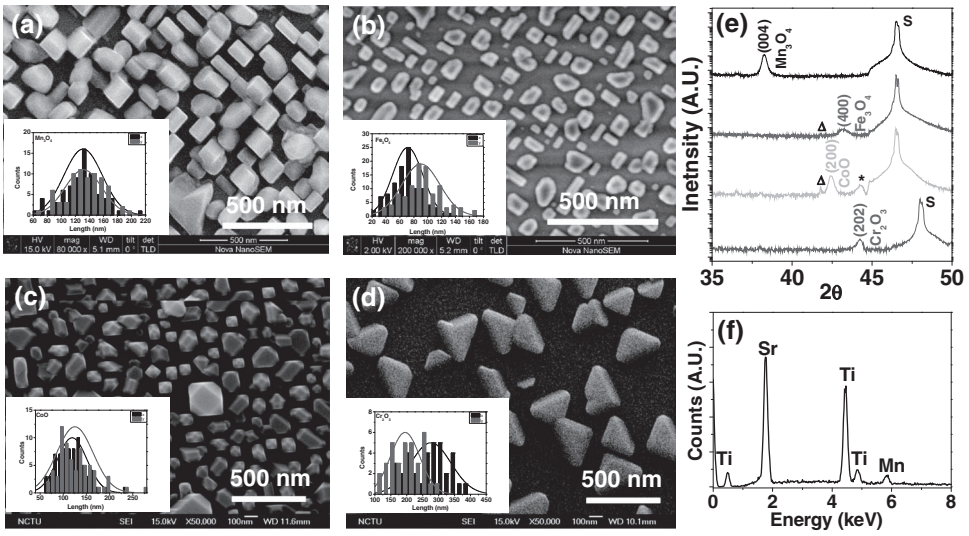

Figure 3. SEM images of a) Mn_3O_4, b) Fe_3O_4, c) CoO and d) Cr_2O_3 nanostructures fabricated on (001) oriented STO substrate ((001)-LAO substrate only for Cr_2O_3). Inset shows their lateral size dispersions. Mn_3O_4 has lateral sizes averaging 130 ± 30 nm, Fe_3O_4 averages 80 nm ± 30 nm, CoO averages 120 ± 35 nm and Cr_2O_3 averages 235 ± 55 nm. The distribution of these lengths in the width (x) and breadth (y). e) XRD patterns of the above mentioned nanostructure (S, Δ and * in the figure represents peaks related with substrate, Cu K_β peak for STO and substrate holder, respectively). f) A representative EDX pattern recorded for the Mn_3O_4/STO system. No trace of Bi is found in the EDX. Similar patterns were seen for each of the other oxides.

rich environment produces oxides and high temperature allow oxides phases to separate. During phase separation the Bi_2O_3 and M-O_x phases are expected to nucleate throughout the film and form dispersed pockets of nanometric size clusters, as illustrated in step II of Figure 2. Once the phase separation is achieved, it is now critical to completely remove Bi_2O_3 from the film. Now one exploits the volatile behavior of Bi_2O_3 at high temperature via controlled cooling of the sample in high vacuum (≈10^{-7} Torr). Moreover, controlled thermodynamic conditions facilitate the individual nanocrystals to attain definite nanocrystal shape, as shown in step III of Figure 2. Eventually it leaves behind isolated M-O_x nanocrystals on the substrate surface, illustrated in step IV of Figure 2. We note that appropriate cooling conditions can be easily tuned to achieve a variety of oxides for multivalent cations.

We now present in detail our results on the synthesis of nanocrystals of Mn_3O_4, Fe_3O_4, CoO, and Cr_2O_3. To demonstrate viability independent of the underlying substrate, (001)-STO and $LaAlO_3$ (LAO) substrates which have significantly different lattice parameters (0.3905 nm and 0.379 nm respectively at room temperatures) were used. **Figure 3** is a panel that shows high magnification SEM images for each of the respective nanostructure sample along with XRD and chemical analysis. Figure 3a is an SEM image of Mn_3O_4 nanocrystals obtained by high temperature deposition (≈860 °C) of $BiMnO_3$ in 35 mTorr oxygen pressure and subsequent controlled cooling of the sample. The SEM image reveals the Mn_3O_4 nanocrystals possess a distinct hut shape. A full analysis of the Mn_3O_4 synthesis and control over shape evolution can be found elsewhere.[28] The corresponding XRD pattern (Figure 3e) confirms that Mn_3O_4 nanostructures are (001) oriented single-crystals. The corresponding cross-section TEM image and the selective area electron diffraction (SAED) is seen in **Figure 4**a. From the SAED pattern we deduce that huts grow in an epitaxial fashion with the epitaxial relationship [100]//[110] direction of STO. Similarly $BiFeO_3$ produces hut shaped Fe_3O_4 nanostructures (Figure 3b), while $BiCoO_3$ and $BiCrO_3$ produce multifaceted CoO and Cr_2O_3 nanostructure respectively (Figure 3c,d).

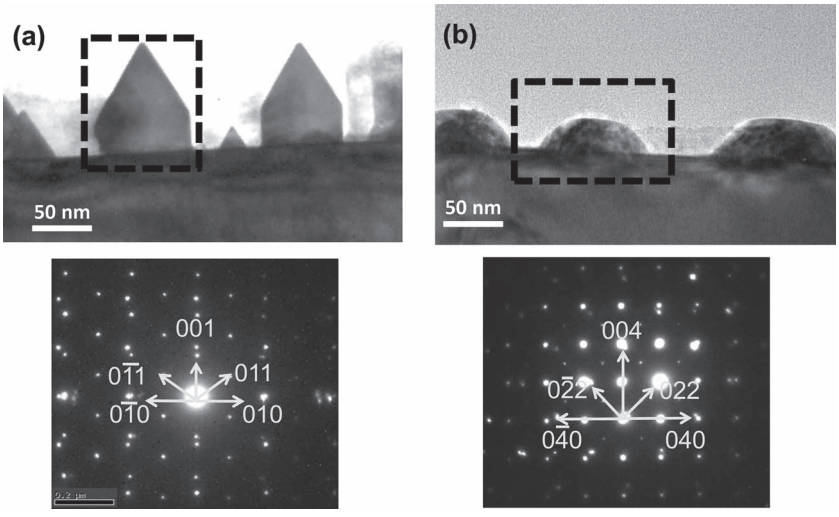

Figure 4. Cross sectional TEM image of a) Mn_3O_4 and b) Fe_3O_4 nanostructures. Selected area electron diffraction patterns (obtained from the square region) of the above nanostructure sample.

Normal coupled θ–2θ XRD scans confirm all nanostructures were found to grow epitaxially on the underlying STO surface (Figure 3e) and (a representative) EDS spot analysis (Figure 3f) shows only the presence of the respective M-O_x element. A wide area XRD scan (not shown) for each metal oxide was also performed to confirm the epitaxial nature of the nanocrystals.

These diverse shapes acquired by the nanostructures are attributed to the interplay between the surface energies of the growing (001) planes of the nanocrystal, the interface energy and the underlying substrate.[32–34] For example, it is well-known that the Hausmannite parent structure has (110) as it's lowest energy plane. Therefore growing along [001] direction, the Mn_3O_4 nanocrystal eventually acquires a hut-shape where the (110) planes bind the nanocrystals as edges of the roof of the hut.

To ascertain that nanocrystal growth indeed occurs by the phase instability process, it is crucial to monitor the phase separation process in situ at synthesis conditions and furthermore confirm bismuth oxide removal from the surface (or M-O_x phase formation) after controlled cooling of the sample. To achieve this, we exploited the presence of a Reflection high-energy electron diffraction (RHEED) gun in the chamber to obtain the electron diffraction pattern at a variety of chamber pressures at the growth temperature conditions. Usually a RHEED pattern is composed of a reflection pattern or spots on a Laue circle (or arc) which signifies an atomically flat sample surface. Such a pattern is shown in **Figure 5**a for the STO substrate. As a monolayer of the film grows on the substrate surface, the spot profile changes to a streaked one, where the brightness of RHEED pattern decreases rapidly because the initial nucleation of the deposited material causes some disorder on the substrate surface.[35] Upon complete monolayer coverage the RHEED pattern returns to back to an arc with distinct spots. Thus, traditionally in reflective-mode the variations in the intensity of a spot with time can then be used to monitor monolayer by monolayer coverage. However in this case we used the RHEED-electron gun in transmission mode to effectively obtain in situ diffraction patterns. In transmission-mode instead of an arc, one observes a regular pattern akin to the one obtained by TEM for single-crystals. Gibert et al. have previously shown RHEED can be exploited to rationalize the expitaxial relationship of $Ce_{1-x}Gd_xO_{2-y}$ nanostructures on (001) LAO substrates.[16] In the present case our use of the RHEED gun in transmission mode gives direct access to crystallographic information that is almost impossible to obtain via conventional diffraction techniques.

Again the case of Mn_3O_4 is first presented in Figure 5. Figure 5a is the pattern from the STO substrate prior to deposition. The bright RHEED spot with a characteristic Laue arc indicates an atomically smooth high-quality STO substrate. During deposition (at 850 °C and 35 mTorr oxygen partial pressure) the intensity of the RHEED spots decreases and spots disappear from the screen. After 600 pulses the patterns change to a streaky one. Here the number of pulses (that is the volume of material) as well as the time is insufficient to give a pattern that confirms phase separation; the streaky pattern however confirms initial growth disorder. However with 2000 pulses (Figure 5c) a clear array of strong and weak (yellow circles) spots are observed. This pattern is stable up to the end of the deposition (Figure 5d, 20000 pulses). In Figure 5e–g we show results for simulated SAEDs obtained using Webemaps for the case of $BiMnO_3$ on $SrTiO_3$ (Figure 5e), Mn_3O_4 on STO (Figure 5f) and Bi_2O_3 on $SrTiO_3$ (Figure 5g).[36] We find that rather than

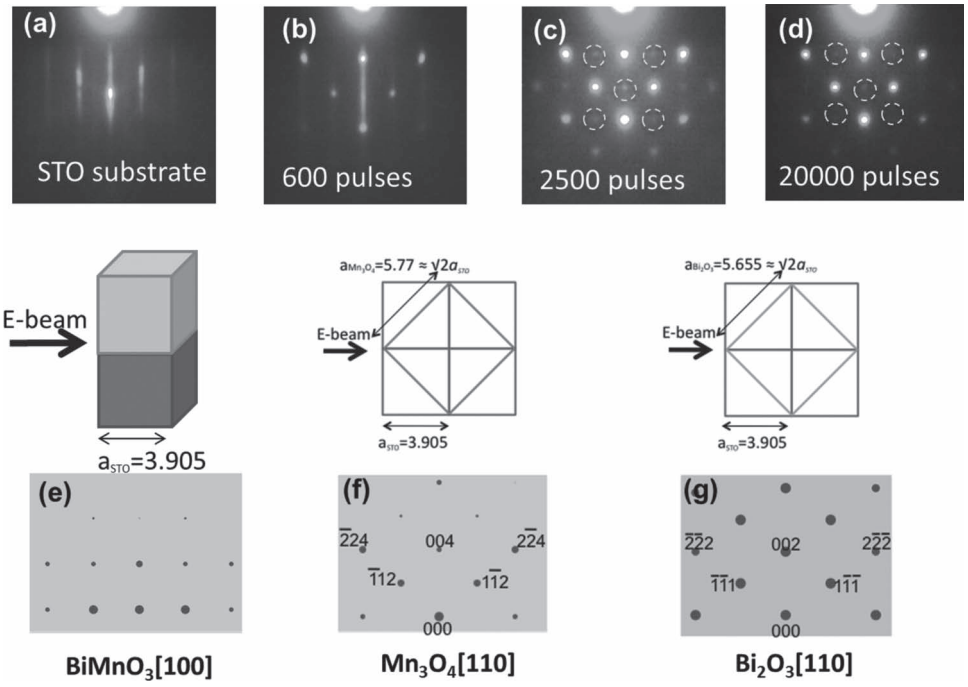

Figure 5. RHEED pattern a) for blank (001)-STO substrate before starting deposition, b) shows the completion of 600 laser pulses, c) with the completion of 2500 laser pulses and formation of Bi_2O_3 diffraction, and d) the completion of deposition and reduction of Bi_2O_3 signatures. Orientation of unit cells of $BiMnO_3$, Mn_3O_4 and Bi_2O_3 on (001)-STO substrate along with it corresponding simulated diffraction patterns in (e), (f), and (g), respectively.

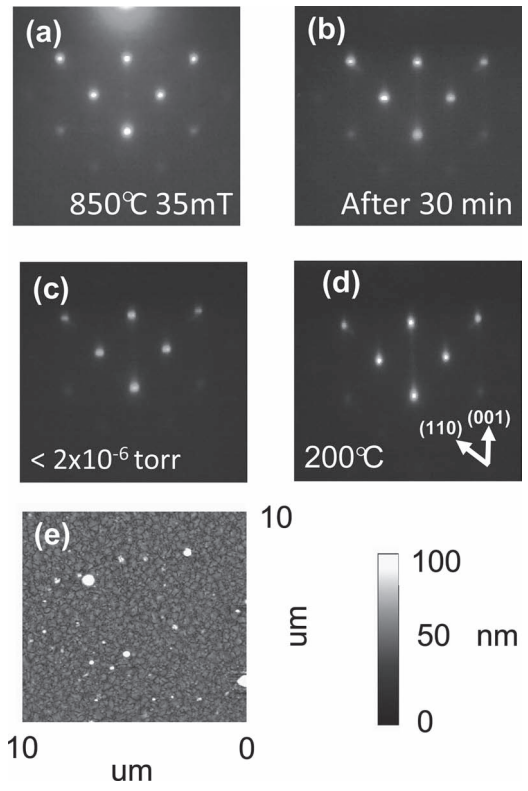

Figure 6. RHEED patterns a) upon the completion of the deposition at growth temperatures and pressure, b) after holding the sample at growth conditions for 30 min, c) after pumping down the chamber to high vacuum conditions at 850 °C and d) captured at 200 °C while cooling the sample in high vacuum. e) The porous films formed by simply growing perovskite ($BiMnO_3$) in vacuum.

$BiMnO_3$, the obtained diffraction pattern from Figure 5c,d match more closely with patterns expected for the two phase-separated components. This proves that the process critically hinges on the breakdown of the perovksite pecursor into the Bi_2O_3–MO_x two-phase mixture. To show that the next step critical step is the volatization of the Bi_2O_3 phase we examine the time-dependence of the RHEED patterns. **Figure 6**a is the pattern immediately after the deposition. Indeed, after holding the sample at growth conditions for 30 minutes, the weak spots begin to disappear (Figure 6b). This must be due to the volatization of Bi_2O_3 and hence the weak spots in Figure 5c,d are attributed to the Bi_2O_3 phase. We thus conclude that the observed diffraction is actually composed of two patterns the strong one belonging to Mn_3O_4 and the weak one to the Bi_2O_3 phase. Figure 6c, which is a pattern obtained after pumping down the chamber to high vacuum conditions at 850 °C and more than 30 minutes shows the weak spots have fully disappeared. Controlled cooling in high vacuum completely evaporates Bi_2O_3 leaving behind only epitaxial Mn_3O_4 phase on the substrate, and hence the presence of only Mn_3O_4 bright spots in the pattern. This is the case in Figure 6d. Thus we confirm the occurrence of phase decomposition of the $BiMnO_3$ precursor on the substrate surface at high temperature. A 45^0 tilt (in the plane of paper) in the transmission spots pattern clearly suggest that one of the crystallographic orientations of Mn_3O_4 is parallel to (110) direction, consistent with the TEM results. These in-situ diffraction patterns also emphasize how critical the step of phase separation is. Indeed, simply growing in vacuum does not result in discrete nanocrystals but rather a very porous film as shown in Figure 6e.

Figure 7 shows the results obtained for the Fe_3O_4, CoO and Cr_2O_3 nanocrystals at their growth temperatures respectively. Figure 7a–c are the RHEED patterns obtained on (001)-STO and LAO substrate before deposition, d–f transmission patterns after complete evaporation of Bi_2O_3 and g–i simulated electron diffraction patterns for respective M-O_x phase. In each case, the resultant diffraction pattern after volatization of the Bi_2O_3 confirms that the oxide nanocrystal as characterized by ex-situ methods (Figure 3,4) are formed right at the growth temperature. A subtle difference in the case of CoO and Cr_2O_3 nanostructures is that the bright spots are aligned parallel to the (001) direction, which indicates no in-plane tilt.

Magnetic characteristics of the magnetic oxides (Fe_3O_4, CoO and Cr_2O_3) were studied via VSM and SQUID. **Figure 8** shows the results of hysteresis loop under room temperature and magnetization (M) as a function of temperature (T) for selective magnetic oxides on (001)-STO substrates for Fe_3O_4 and CoO and on (001)-LAO substrates for Cr_2O_3. All the diagrams are shown after subtracting the weak antiferromagnetic contribution from substrates. In order to investigate the low

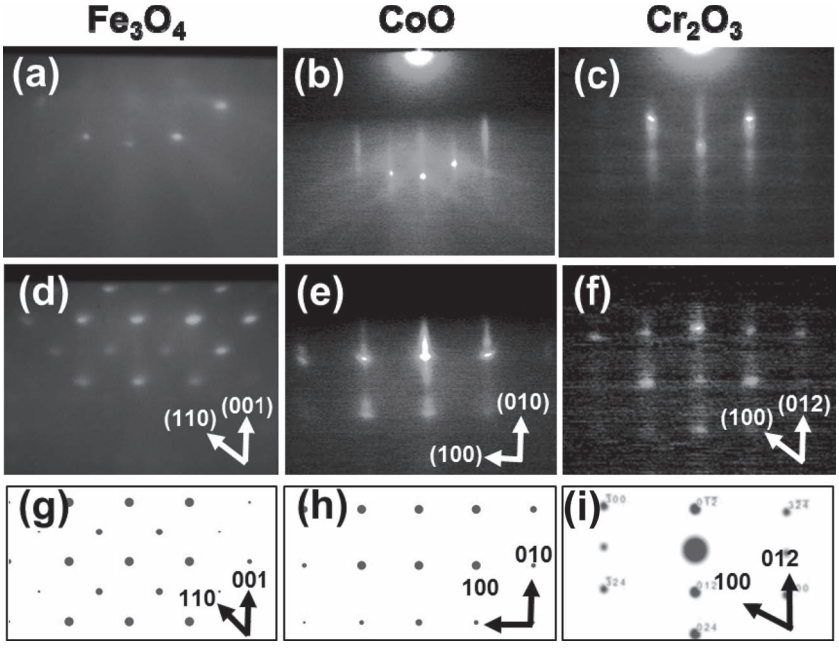

Figure 7. RHEED patterns for a–c) blank substrate before starting deposition conditions (LAO for Cr_2O_3 and STO for rest) and transmission patterns d–f) after cooling the sample in high vacuum for Fe_3O_4, CoO and Cr_2O_3, nanostructures, respectively, and g–i) simulated electron diffraction patterns for the aforementioned metal oxides.

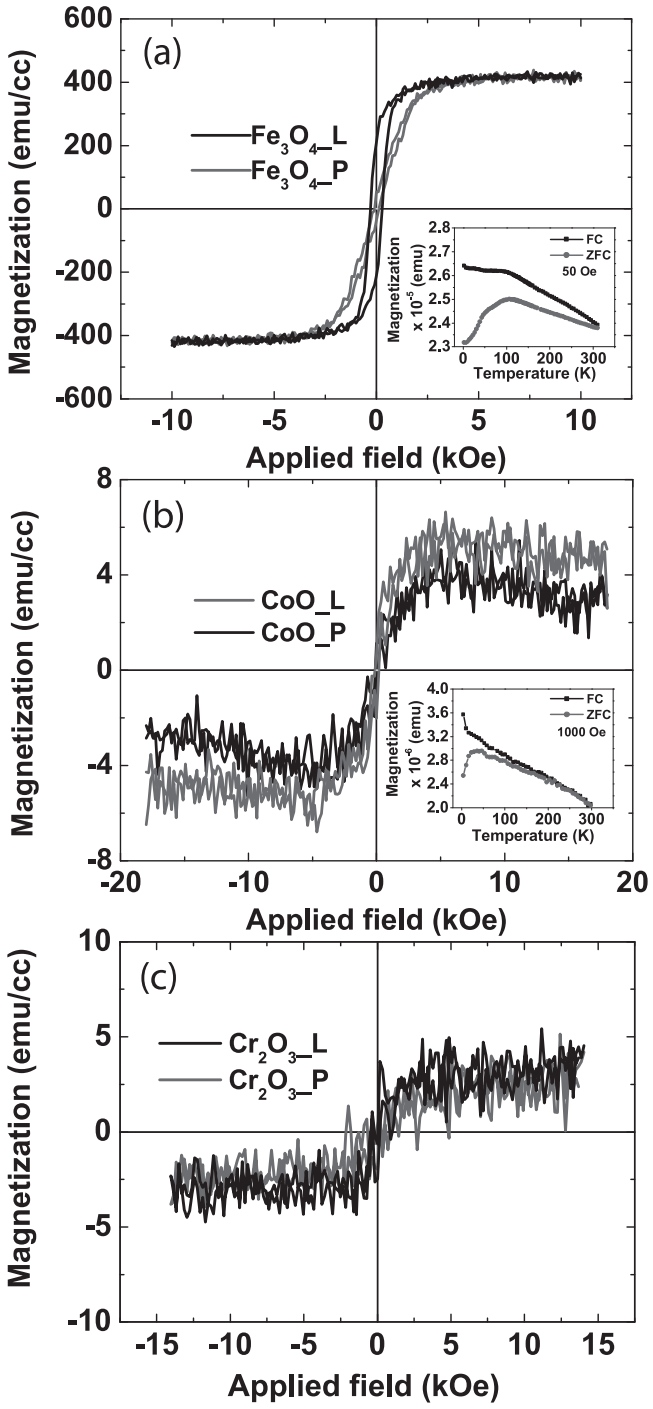

Figure 8. Magnetic characterization of chosen nanostructure. Curves labelled "L" represent measurements performed in the lateral direction of the nanostructures and "P" to represent measurements perpendicular to the structures. Hysteresis loop of a) Fe_3O_4, b) CoO, c) and Cr_2O_3 nanostructures is measured via VSM under RT. Insets show magnetization vs. temperature measurement of respective nanostructures conducted via SQUID.

temperature magnetic behaviour, magnetization vs. temperature (MT) measurements have been conducted on the representative samples by the zero-field cooling (ZFC) and field cooling (FC) procedure to 4 K and then measuring under a dc magnetic field (H) following the increasing temperature. For Fe_3O_4 (Figure 8a), coercivity values (Hc) of 298 Oe and 97 Oe were observed in the magnetic hysteresis in-plane (L) and out-of-plane (P) respectively. It was found the easy axis of magnetic moment lay in the in-plane direction, along the lateral edges of Fe_3O_4 nanostructure. It is widely known that the ferromagnetic behaviour of Fe_3O_4 bulk magnetite possesses the coercivity of 115–150 Oe in average.[37] By comparison with bulk Fe_3O_4, the enhanced coercivity in as-grown direction of Fe_3O_4 nano-pillars may be attributed to shape anisotropy which is the dominant magnetic anisotropy in our nanostructure. Moreover, the low temperature MT curve is shown in inset of Figure 8a. The magnetization increases with temperature and reaches the maximum value at 106 K, identified as the blocking temperature (T_B). This temperature indicates the magnetic transition between ferro- and superparamagnetic orders. Below T_B, ZFC (red line) curve shows the mounted magnetization resulted from gradual moment reorientation along applied field.

CoO is a well-known antiferromagnetic insulator at room temperature, which manifests a weak response to MH measurement at 300 K (Figure 8b). If we perform the MT measurement on CoO samples (inset in Figure 8b), the magnetization value remains feeble but increases gradually with decreasing T. As the temperature reaches around 35 K, the CoO behaves the maximum of moment in ZFC (red line) measurement and keeps mounting in FC (blue line) measurement, a phenomenon that is usually related to T_B temperature in nano-scaled AFM insulators.[38] Lastly, the magnetic properties of Cr_2O_3 nanostructures are illustrated in Figure 8c. Our nanoscaled Cr_2O_3, again, exhibits a disparate behavior: a weak but real magnetization moment under 5000 Oe dc magnetic field in room temperature. While bulk chromium (III) oxide is characterized as an antiferromagnetic material with a Neel temperature (T_N) about 307 K,[39] there is no sign of either a strong peak or slope change in MT curve which would identify the T_N. Thus we observe physical behavior in these magnetic oxide nanocrystals that is distinct from bulk. This suggests a strong potential to design new functional devices based on the self-assembly. For example, we are exploring the possibility to create core-shelled architectures for exchange bias applications and these will be reported in the near future.

3. Conclusion

In summary, we have demonstrated a facile approach to fabricate phase pure and epitaxial metal oxide nanostructures on oxide supports via phase separation and evaporation approach from a parent bismuth perovskite precursor. By monitoring in-situ RHEED patterns, we have systematically shown the occurrence of phase separation of Bi_2O_3 and M-O_x in the deposited Bi-M-O_x film at high temperature. Controlled cooling in high vacuum leads to complete evaporation of Bi_2O_3 leaving behind, a self-assembled array of metal oxide nanostructures. This approach was applied to $BiMnO_3$, $BiFeO_3$, $BiCoO_3$, $BiCrO_3$ precursors to obtain epitaxial Mn_3O_4, Fe_3O_4, CoO and Cr_2O_3 nanostructures. The obtained nanocrystals show magnetic behavior that is distinct from their bulk counterparts and offer considerable promise for spintronic applications.

4. Experimental Section

Epitaxial nanostructures of metal oxide were grown on polished (001)-STO procured from SHINKOSHA, Japan using pulsed laser deposition (PLD) with a KrF (λ = 248 nm) excimer laser and energy density in the range from 1 to 1.8 J/cm^2. 99.95% pure stoichiometric targets of Bi-M-O$_x$, where M = Mn, Fe, Co and Cr were employed. Depositions were carried out at oxygen pressures in the range of 10 to 100 mTorr and substrate temperature in the range from 825 to 900 °C. After deposition, samples were cooled down to room temperature in high vacuum (≈10^{-7} Torr) at a cooling rate of 5 °C/min. In-situ reflection high-energy electron diffraction (RHEED) patterns were obtained with a STAIB Instruments system using an electron beam of 20 kV and an incidence angle of 2–5° with respect to the substrate surface. The Nanostructured samples were characterized using scanning electron microscopy (SEM), energy dispersive spectroscopy (EDS), cross-section transmission electron microscopy (TEM), atomic force microscopy (AFM) and x-ray diffraction (XRD) techniques. Magnetic properties were tested using vibrating sample magnetometer (VSM) and semiconductor quantum interface device (SQUID) techniques.

Acknowledgements

The research at UNSW was supported in part by an Australia-India DIISR and ARC Discovery and LIEF Grant. The research at National Chiao Tung University was supported by the National Science Council, R.O.C (under contract NSC 100-2119-M-009-003), National Science Council, Taiwan, (under contract No. NSC-101–2119-M-009–003-MY2), Ministry of Education (under grant No. MOE-ATU 101W961), and Center for interdisciplinary science of National Chiao Tung University. N.V. acknowledges the support of the EPSRC for his visit to Queen's University Belfast.

Received: April 17, 2012
Published online: July 31, 2012

[1] K. Nagashima, T. Yanagida, K. Oka, M. Taniguchi, T. Kawai, J.-S. Kim, B. H. Park, *Nano Lett.* **2010**, *10*, 1359.
[2] C. s. Moreno, C. Munuera, S. Valencia, F. Kronast, X. Obradors, C. Ocal, *Nano Lett.* **2010**, *10*, 3828.
[3] Z. P. Wei, M. Arredondo, H. Y. Peng, Z. Zhang, D. L. Guo, G. Z. Xing, Y. F. Li, L. M. Wong, S. J. Wang, N. Valanoor, T. Wu, *ACS Nano* **2010**, *4*, 4785.
[4] C. Ross, *Ann. Rev. Mater. Res.* **2001**, *31*, 203.
[5] D. Li, W. Y. Teoh, J. J. Gooding, C. Selomulya, R. Amal, *Adv. Funct. Mater.* **2010**, *20*, 1767.
[6] C. Marichy, M. Bechelany, N. Pinna, *Adv. Mater.* **2012**, *24*, 1017.
[7] C. Baratto, E. Comini, G. Faglia, G. Sberveglieri, M. Zha, A. Zappettini, *Sens. Actuators B* **2005**, *109*, 2.
[8] M. P. Sharrock, *J. Appl. Phys.* **1994**, *76*, 6413.
[9] S. Akihito, *Mater. Today* **2008**, *11*, 28.
[10] A. P. Alivisatos, *Science* **1996**, *271*, 933.
[11] A. N. Goldstein, C. M. Echer, A. P. Alivisatos, *Science* **1992**, *256*, 1425.
[12] J. Park, K. An, Y. Hwang, J.-G. Park, H.-J. Noh, J.-Y. Kim, J.-H. Park, N.-M. Hwang, T. Hyeon, *Nat. Mater.* **2004**, *3*, 891.
[13] V. F. Puntes, K. M. Krishnan, A. P. Alivisatos, *Science* **2001**, *291*, 2115.
[14] R. F. Service, *Science* **1996**, *271*, 920.
[15] Y. Yin, A. P. Alivisatos, *Nature* **2005**, *437*, 664.
[16] M. Gibert, T. Puig, X. Obradors, A. Benedetti, F. Sandiumenge, R. Hühne, *Adv. Mater.* **2007**, *19*, 3937.
[17] N. Wang, L. Guo, L. He, X. Cao, C. Chen, R. Wang, S. Yang, *Small* **2007**, *3*, 606.
[18] C. Moreno, P. Abellán, A. Hassini, A. Ruyter, A. P. del Pino, F. Sandiumenge, M.-J. Casanove, J. Santiso, T. Puig, X. Obradors, *Adv. Funct. Mater.* **2009**, *19*, 2139.
[19] T. Yu, J. Moon, J. Park, Y. I. Park, H. B. Na, B. H. Kim, I. C. Song, W. K. Moon, T. Hyeon, *Chem. Mater.* **2009**, *21*, 2272.
[20] M. Batzill, K. Katsiev, J. M. Burst, U. Diebold, A. M. Chaka, B. Delley, *Phys. Rev. B* **2005**, *72*, 165414.
[21] C. H. Lee, R. F. C. Farrow, C. J. Lin, E. E. Marinero, C. J. Chien, *Phys. Rev. B* **1990**, *42*, 11384.
[22] I. E. Wachs, J.-M. Jehng, W. Ueda, *J. Phys. Chem. B* **2004**, *109*, 2275.
[23] R. Ramesh, N. A. Spaldin, *Nat. Mater.* **2007**, *6*, 21.
[24] G. Catalan, J. F. Scott, *Adv. Mater.* **2009**, *21*, 2463.
[25] S. Fujino, M. Murakami, S.-H. Lim, L. G. Salamanca-Riba, M. Wuttig, I. Takeuchi, *J. Appl. Phys.* **2007**, *101*, 013903.
[26] H. Bea, M. Bibes, A. Barthelemy, K. Bouzehouane, E. Jacquet, A. Khodan, J.-P. Contour, S. Fusil, F. Wyczisk, A. Forget, D. Lebeugle, D. Colson, M. Viret, *Appl. Phys. Lett.* **2005**, *87*, 072508.
[27] E. Langenberg, M. Varela, M. V. García-Cuenca, C. Ferrater, F. Sánchez, J. Fontcuberta, *Mater. Sci. Eng. B* **2007**, *144*, 138.
[28] K. A. Bogle, V. Anbusathaiah, M. Arredondo, J.-Y. Lin, Y.-H. Chu, C. O'Neill, J. M. Gregg, M. R. Castell, V. Nagarajan, *ACS Nano* **2010**, *4*, 5139.
[29] M. Murakami, S. Fujino, S.-H. Lim, L. G. Salamanca-Riba, M. Wuttig, I. Takeuchi, B. Varughese, H. Sugaya, T. Hasegawa, S. E. Lofland, *Appl. Phys. Lett.* **2006**, *88*, 112505.
[30] V. Anbusathaiah, C. J. Cheng, S. H. Lim, M. Murakami, L. G. Salamanca-Riba, I. Takeuchi, V. Nagarajan, *Appl. Phys. Lett.* **2008**, *93*, 192906.
[31] U. Lüders, F. Sánchez, J. Fontcuberta, *Phys. Rev. B* **2004**, *70*, 045403.
[32] W. L. Winterbottom, *Acta Metallurg.* **1967**, *15*, 303.
[33] H. Zheng, F. Straub, Q. Zhan, P.-L. Yang, W.-K. Hsieh, F. Zavaliche, Y.-H. Chu, U. Dahmen, R. Ramesh, *Adv. Mater.* **2006**, *18*, 2747.
[34] N. Dix, R. Muralidharan, J.-M. Rebled, S. Estradé, F. Peiró, M. Varela, J. Fontcuberta, F. Sánchez, *ACS Nano* **2010**, *4*, 4955.
[35] A. Ichimiya, P. I. Cohen, *Reflection high energy electron diffraction*, Cambridge University Press, Cambridge **2004**.
[36] J. M. Zuo, J. C. Mabon, *Microsc. Microanal.* **2004**, *10*, http://http://emaps.mrl.uiuc.edu/.
[37] J. Smith, H. P. J. Wijn, *Ferrites*, John Wiley and Sons, New York **1959**.
[38] T. Ambrose, C. L. Chien, *Phys. Rev. Lett.* **1996**, *76*, 1743.
[39] M. Catti, G. Sandrone, G. Valerio, R. Dovesi, *J. Phys. Chem. Solids* **1996**, *57*, 1735.